Facile fabrication of MOF-derived octahedral CuO wrapped 3D graphene network as binder-free anode for high performance lithium-ion batteries

Dong Ji [a], Hu Zhou [b,*], Yongli Tong [a], Jinpei Wang [a], Meizhou Zhu [b], Tianhui Chen [a], Aihua Yuan [a,c,*]

[a] School of Environmental and Chemical Engineering, Jiangsu University of Science and Technology, Zhenjiang 212003, PR China
[b] School of Material Science and Engineering, Jiangsu University of Science and Technology, Zhenjiang 212003, PR China
[c] Marine Equipment and Technology Institute, Jiangsu University of Science and Technology, Zhenjiang 212003, PR China

HIGHLIGHTS

- A facile strategy to fabricate 3DGN/MOF-derived metal oxide was proposed.
- 3DGN/CuO was used as electrode of energy storage devices for the first time.
- The electrode showed excellent electrochemical properties for lithium-ion batteries.

GRAPHICAL ABSTRACT

The 3DGN/MOF-derived CuO composite was used as lightweight and binder-free anode material for Li-ion batteries, exhibiting a high gravimetric capacity and large reversible areal capacity, superior rate capacity and excellent cycling performance.
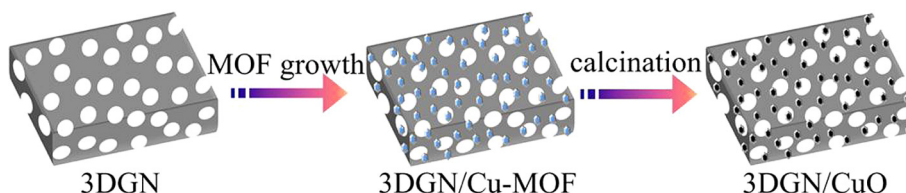
ARTICLE INFO

ABSTRACT

In this work, an effective and facile strategy to fabricate binder-free electrodes composing 3D graphene network (3DGN) and octahedral CuO has been proposed. In this design, Cu-based MOF crystals were first uniformly grown on the surface of 3DGN substrate through a solution immersion method and then a subsequent thermal treatment isolated the formation of well-dispersed nanostructured CuO octahedras wrapped 3DGN. The obtained 3DGN/CuO composites were utilized as binder-free anodes of lithium-ion batteries for the first time, yielding a high reversible gravimetric capacity of 409 mAh g^{-1} (a large areal capacity of 0.39 mAh cm^{-2}) at 100 mA g^{-1}, excellent cyclability with 99% capacity retention after 50 cycles and superior rate capability of 219 mAh g^{-1} at 1600 mA g^{-1}. The remarkable performance of the composite electrode can be reasonably attributed to the synergistic interaction between octahedral CuO nanoparticles with high capacity and the conductive 3D graphene network with a large surface area and an interconnected porous structure.

1. Introduction

Rechargeable lithium-ion batteries (LIBs) have attached significant interest during the past decades due to their applications in portable electronic devices, clean energy storage and hybrid electric vehicles [1]. Considerable efforts have been dedicated to seek ideal electrode materials for improving the lithium reversible storage capacities and stabilities of LIBs [2]. Transition metal oxides (e.g. MnO$_2$ [3,4], Fe$_3$O$_4$ [5,6], Fe$_2$O$_3$ [7,8], CuO [9,10], NiO [11,12], SnO$_2$ [13,14], Co$_3$O$_4$ [15,16], TiO$_2$ [17,18]) have been investigated intensively as one of the most promising anode candidates for next-generation high-performance LIBs because of their higher theoretical capacities (500–1000 mAh g^{-1}) than commercial graphite (372 mAh g^{-1}), natural abundance, nontoxic nature and low

cost. However, the low inherent conductivities and large volume change of metal oxides during the discharge/charge process yielded the poor cycling stabilities and low rate capabilities. To address these issues, tremendous efforts have been developed to improve the structural integrities and electrical conductivities of metal oxides-based anode materials such as optimizing particle size or morphology and fabricating carbon hybrids [19,20].

In recent years, metal-organic frameworks (MOFs) have been successfully employed as effective sacrificial templates or precursors to construct different kinds of nanostructured metal oxides or porous carbon with intriguing properties through the pyrolysis process because of their high specific surface areas and tunable pore structures [21–28]. Especially, the resulting MOF-derived metal oxides can be size- or shape-controlled under well-adjusted preparation conditions. For example, spindle-like porous α-Fe$_2$O$_3$ [29], hollow Co$_3$O$_4$ dodecahedra [30,31], hollow CuO octahedral [32] and porous anatase TiO$_2$ [33], etc., were fabricated using suitable MOFs as the precursors and these metal oxides displayed excellent electrochemical properties. To improve the electronic conductivity and mechanical strain of metal oxides, nanostructured carbon materials (carbon nanofibers [34,35], carbon nanotubes [36–38], graphene sheets [39–43], etc.) were employed to incorporate with metal oxides, where carbon materials acted as conductive networks to increase the electrical conductivities and as volume buffers to alleviate internal stress during the discharge/charge process.

As we all know, continuous and interconnected three-dimensional graphene network (3DGN) grown on nickel foam has been synthesized and recognized widely as an excellent current collector in the energy storage and conversion fields owning to its extremely light weight, excellent electrical conductivity, large internal surface area, macroscopically porous structure, high mechanical strength and flexibility, as well as the rapid mass and electron transport kinetics for Li ions [44]. 3DGN coated with metal oxides can be used as binder-free electrode materials for LIBs, and delivered much higher electrochemical activities compared to those of bare metal oxides [45]. Motivated by the merits of MOF-derived metal oxides and 3DGN, it was anticipated that such type of composite, hereinafter designed as 3DGN/MOF-derived metal oxides, would improve the electrochemical performance of anode electrodes of LIBs. Unfortunately, there are few examples of 3DGN/MOF-derived metal oxides so far. Zhang reported a two-step annealing strategy for the synthesis of 3DGN/metal oxides (ZnO, Fe$_2$O$_3$) hybrids by employing MOFs (ZIF-8, MIL-88) as sacrificial templates and precursors [46]. The obtained 3DGN/Fe$_2$O$_3$ composite has achieved impressive electrochemical properties. Very recently, our group applied a facile strategy to prepare 3DGN supported Mn$_2$O$_3$ with a nanowire stacking flower-like morphology using Mn-based MOF as the precursor and this composite was used as free-standing electrodes for high-performance supercapacitors [47].

Along with the research line of MOF-graphene and their derivatives for the energy-storage application conducted by our group [48–51], we described here a two-step process to fabricate 3DGN cross-linked with nanostructured CuO octahedras. In this design, Cu-based MOF particles were first uniformly grown on the surface of 3DGN through a solution immersion method. Then, a subsequent thermal treatment isolated the formation of CuO octahedras wrapped 3DGN. The as-prepared 3DGN/CuO hybrid was directly explored as anode materials for LIBs without any binder or further treatment, yielding a high reversible gravimetric and areal capacity, excellent cyclability and superior rate capability. To the best of our knowledge, until now there has been no report on the rational design and preparation of 3D graphene network supported CuO particles for the energy storage application. Such remarkable electrochemical performances can be ascribed to the synergistic

effect between uniformly dispersed nanostructured CuO octahedras and the conductive 3DGN with interconnected porous architecture.

2. Experimental

2.1. Chemical reagents

Nickel foams were purchased from Shenzhen Six Carbon Technology, China. All other chemical reagents were purchased from Sigma-Aldrich and used directly without further purification.

2.2. Synthesis of 3DGN

3DGN was synthesized by chemical vapor deposition (CVD). Briefly, the nickel foam placed into a quartz tube was heated to 1000 °C at a 30 °C min^{-1} heating rate and maintained for 60 min under atmospheric pressure with a gas flow of Ar (300 sccm) and H$_2$ (10 sccm). Then CH$_4$ (60 sccm) was bubbled into the chamber with a mixing gas of Ar/H$_2$ (V/V = 100/10) for 30 min. The furnace was rapidly cooled down to room temperature at a rate of 100 °-C min^{-1} under of Ar/H$_2$ flow, and the graphene on nickel foam was obtained. To remove the metallic Ni, the as-prepared sample was immersed in a mixture solution of FeCl$_3$ (1 mol L^{-1}) and HCl (1 mol L^{-1}) at room temperature for 3.5 h. Finally as-obtained 3DGN was heated in 69 wt% HNO$_3$ at 80 °C for 8 h and subjected to further use.

2.3. Synthesis of Cu-BTC

Cu-based MOF was prepared by a typical procedure reported elsewhere with slight modifications [32]. 7.28 g Cu(NO$_3$)$_2$·3H$_2$O was dissolved in a 40 mL methanol to give solution **A**, while 3.5 g of 1,3,5-benzenetricarboxylic acid (H$_3$BTC) and 0.8 g PVP (K-30) were both dissolved in a 40 mL methanol to form solution **B**. After that, solution **A** was transferred slowly into solution **B**. The blue precipitations appeared after the reaction mixture was kept at room temperature for 3.5 h. The products were collected by centrifugation, washed with methanol several times, and then dried in an oven at 60 °C. The resultant material was referred to Cu-BTC.

2.4. Synthesis of CuO

CuO was prepared through the calcination of the Cu-BTC precursor in a furnace under a flow of air. The temperature was firstly raised to 320 °C at a ramping rate of 1 °C min^{-1}, and then stabilized at 320 °C for 2 h. Upon cooling down to room temperature, the black CuO powders were harvested.

2.5. Synthesis of 3DGN/Cu-BTC

The acid-treated 3DGN (1 cm × 1 cm) was placed in a glass bottle. 2 mL of solution **B** mentioned above was added, followed by the slow adding of solution **A** (2 mL). The bottle was shaken gently for 30 s and stood for 3.5 h. The resulting 3DGN/Cu-BTC composite was washed with methanol several times, and dried in an oven at 60 °C. The color of 3DGN changed to blue, indicating the growth of Cu-BTC crystals on the surface of 3DGN.

2.6. Synthesis of 3DGN/CuO

The 3DGN/CuO composite was prepared through the calcination of 3DGN/Cu-BTC precursors in a furnace under a flow of air. The temperature was raised to 320 °C at a ramping rate of 1 °C min^{-1}, and then stabilized at 320 °C for 2 h. Upon naturally

cooling down to room temperature, the resulting 3DGN/CuO products were obtained. The color of bulk material was found from blue to black, confirming the formation of 3DGN wrapped with CuO particles.

2.7. Material characterization

The structures of as-prepared samples were recorded on a Shimadzu XRD-6000 diffractometer using Cu-K$_\alpha$ radiation. Raman spectra were collected on a Renishaw in Via Raman spectroscopy with excitation at 532 nm laser. The surface electronic states were investigated by X-ray photoelectron spectroscopy (XPS, Thermo-Fisher Scientific ESCALAB250Xi using Al-K$_\alpha$ radiation) with a base pressure of 5×10^{-10} mbar. The morphology and microstructure of the materials were investigated by field-emission scanning electron microscopy (FE-SEM, ZEISS Merlin Compact) and field-emission transmission electron microscopy (FE-TEM, JEOL JEM-2100F). The elemental mapping analysis was conducted on an energy-dispersive X-ray spectrometry (EDS, Oxford X-Max). The N$_2$ adsorption-desorption isotherm of pure CuO was recorded at 77 K on a BEL (Japan, Inc.) instrument. The samples were outgassed under vacuum at 453 K for 12 h prior to the adsorption measurement. The Brunauer-Emmett-Teller (BET) specific surface area was calculated from the adsorption data, and the pore diameter distribution curves were determined using the Barrett-Joyner-Halenda (BJH) method. The mass of as-prepared samples were weighted 3 times by an electronic balance with a resolution of 0.01 mg and an average value was used. The weight values were obtained by calculating the mass difference before and after growth of Cu-BTC or CuO particles. For the 3DGN/Cu-BTC composite, the mass of 3DGN and Cu-BTC were 0.65 and 1.05 mg, respectively, and the mass of 3DGN/Cu-BTC per area was calculated to be 1.70 mg cm^{-2}. The standard deviations of 3DGN and Cu-BTC were 0.0125 and 0.017, respectively. According to the similar calculation method, the mass of 3DGN and CuO in the 3DGN/CuO composite were 0.65 and 0.30 mg, respectively, and the mass of 3DGN/CuO was 0.95 mg cm^{-2}. The standard deviations of 3DGN and CuO were 0.0125 and 0.0082, respectively. The weight fraction of CuO in the composite was about 31.6%.

2.8. Electrochemical measurements

Electrochemical measurements were carried out by using CR2032-type coin cells, and the cells were assembled in an argon-filled glove-box. Celgard 2600 was used as the separator, metallic lithium foil as the counter electrode, and 1 M LiPF$_6$ in ethylene carbonate/diethyl carbonate (1:1 by volume) as the electrolyte. The as-prepared 3DGN, 3DGN/Cu-BTC and 3DGN/CuO samples were used directly as the working electrodes without adding any conductive agent or binding materials. In the control experiment, the pure Cu-BTC and CuO were mixed with super-p and polyvinylidene fluoride (PVDF) binder at a weight ratio of 75:15:10 in N-methyl-2-pyrrolidone (NMP), respectively. The as-made slurry was coated onto the copper foil substrate and dried at 60 °C for 12 h. The galvanostatic discharge/charge measurements were carried out on a LAND CT 2001A battery system. Capacity values were based on the total mass of the active material. The active material in the composite should be 3DGN/CuO because both components contributed the capacity values of the final composite, while the active material should be CuO for the electrode of pure CuO. The cyclic voltammetry (CV) was measured by using a CHI660D electrochemical workstation (Chenhua, Shanghai, China) over the voltage range 0.01–3.0 V at a 0.2 mV s^{-1} scan rate. The electrochemical impedance spectroscopy (EIS) measurements were recorded by using an Autolab system (Metrohm) in

the frequency range from 0.1 Hz to 100 kHz at open circuit potential by applying an ac voltage of 10 mV amplitude.

3. Results and discussion

Fig. 1a and b displayed the XRD patterns of all as-prepared products. The significant diffraction peak at $2\theta = 26.5°$ for 3DGN can be attributed to the (0 0 2) reflection of graphitic carbon (JCPDS 75-1621). All diffraction peaks of as-obtained Cu–BTC were in good agreement with the reported results [52], indicating the successful preparation of the same MOF formulated as HKUST-1 (Cu$_3$(BTC)$_2$). The characteristic peaks of 3DGN and Cu-BTC were obviously observed in the diffraction patterns of 3DGN/Cu-BTC, confirming the combination of both components. The diffraction peaks of copper oxide resulting from annealing Cu-BTC precursors were perfectly assigned to the monoclinic phase of CuO (JCPDS 48-1548, space group $C2/c$, $a = 4.682$, $b = 3.427$, $c = 5.132$). No impurity phases were found in diffraction patterns, revealing a complete thermal conversion of Cu-BTC into CuO. All diffraction peaks of the 3DGN/CuO composite can be well indexed to copper oxide except for the peak at $2\theta = 26.5°$ from the 3DGN substrate, which demonstrated that crystalline CuO particles has been integrated into the framework of 3DGN after the thermal treatment of 3DGN/Cu-BTC. The broad diffraction peaks associated with CuO indicated the small crystallite size, as described in the morphological analysis below.

The Raman spectra of 3DGN and 3DGN/CuO were displayed in Fig. 1c and d. 3DGN showed pronounced G and 2D bands at around 1582 and 2688 cm^{-1}, respectively. The absence of D band at about 1350 cm^{-1} indicated that the CVD-grown graphene network of high-quality with few defects and distorted carbon, which is favorable for improving the electrical conductivity [53]. The relatively low integral ratio of G to 2D band implied that the 3DGN consists of few-layered graphene sheets [54]. Raman spectrum in the low wavelength region of 3DGN/CuO was shown in Fig. 1d. The peak with a relatively high intensity at 299 cm^{-1} was assigned to A$_g$ mode and two peaks at 348 and 626 cm^{-1} corresponded to 2B$_g$ modes according to the vibrational spectra of CuO single crystal, confirming that the copper oxide nanostructures on 3DGN have a single phase [55–58].

The survey XPS spectra (Fig. 2a) revealed the co-existence of carbon, oxygen, and copper elements in the as-produced 3DGN/CuO composite. The peak at 284.8 eV in the high-resolution XPS spectrum (Fig. 2b) of C 1s was originated from the sp^2-hybridized carbon atoms from 3DGN [59]. Two distinct peaks located at 934.0 eV and 954.3 eV in the XPS spectrum (Fig. 2c) of Cu 2p corresponded to the Cu 2p$_{3/2}$ and 2p$_{1/2}$ spin-orbit states, respectively. The spin energy separation was 20.3 eV, in agreement with those reported for CuO, indicating +2 oxidation state for Cu in the composite [55,56,60]. In the high-resolution spectrum of O 1 s, the peak at 532.1 eV was related to O—C (O 1s) of the graphene sheet [61], while the peak at 530.2 eV can be ascribed to O—Cu (O 1s) of CuO [55,56].

The morphology and structure of as-prepared products were examined by SEM and TEM, as shown in Fig. 3a. The CVD-growth graphene replicated the 3D network and porous structure of Ni foam after removal of the Ni template, without collapsing and cracking (Figs. S1 and S2). The pure Cu-BTC crystals displayed an octahedral shape with an edge length of 200–400 nm (Fig. 3b). After the calcination of Cu-BTC in air, the resulting CuO particles remained the similar size and shape to Cu-BTC. However, the surface of CuO particles became more textured and rougher than Cu-BTC due to the release of organic parts during the calcination. After the in-situ growth of MOF crystals, the morphology of 3DGN showed no obvious difference except for the color change from
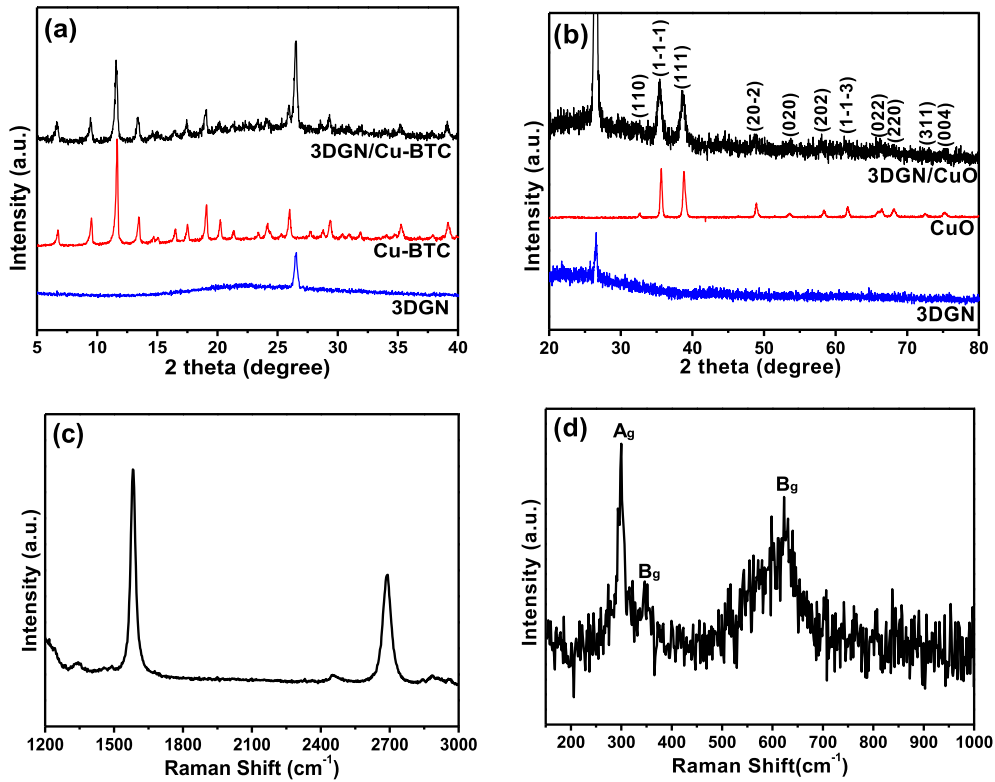
Fig. 1. Powder XRD patterns of (a) 3DGN/Cu-BTC and (b) 3DGN/CuO systems, and Raman spectra of (c) 3DGN and (d) the 3DGN/CuO in the region of 150–1000 cm^{-1}.
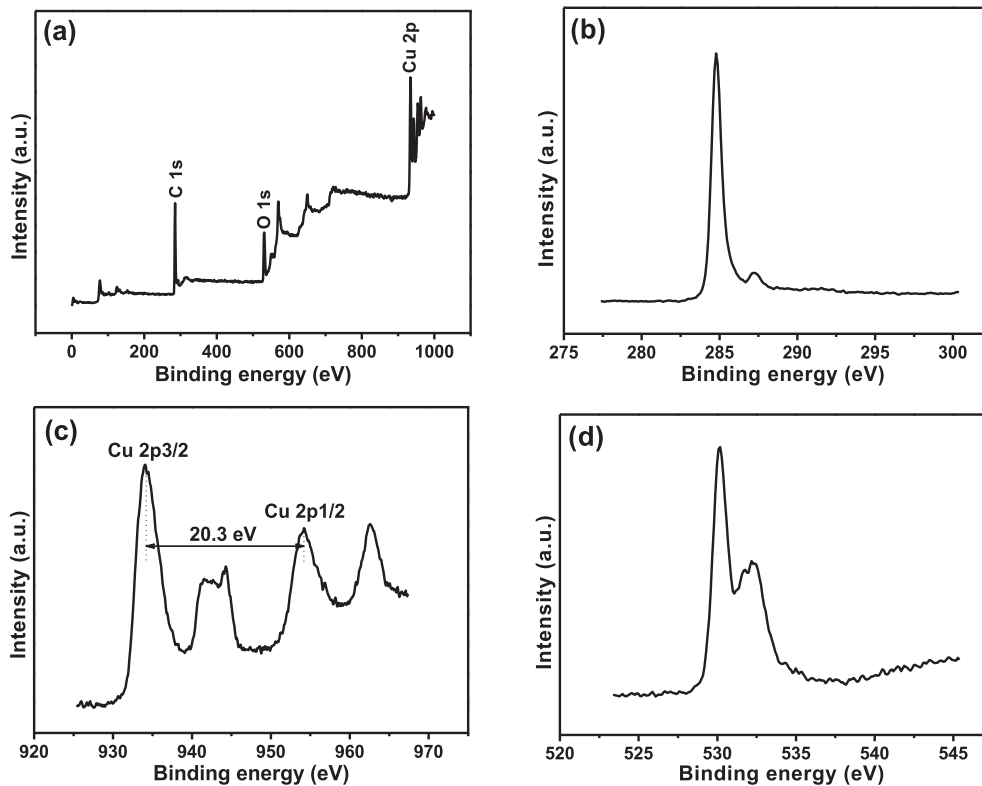

Fig. 2. XPS spectra of the 3DGN/CuO composite: (a) Survey spectrum, (b) C 1s spectrum, (c) Cu 2p spectrum, and (d) O 1s spectrum.

black to blue, as well as the rougher surface (Fig. 3d) than pure 3DGN. It could be clearly observed from Fig. 3e that Cu-BTC particles were uniformly and densely wrapped in the entire skeleton of 3DGN. These particles present less aggregation because of the confinement of 3DGN and the intact contact between Cu-BTC and graphene network. Interestingly, there was a slight difference in the
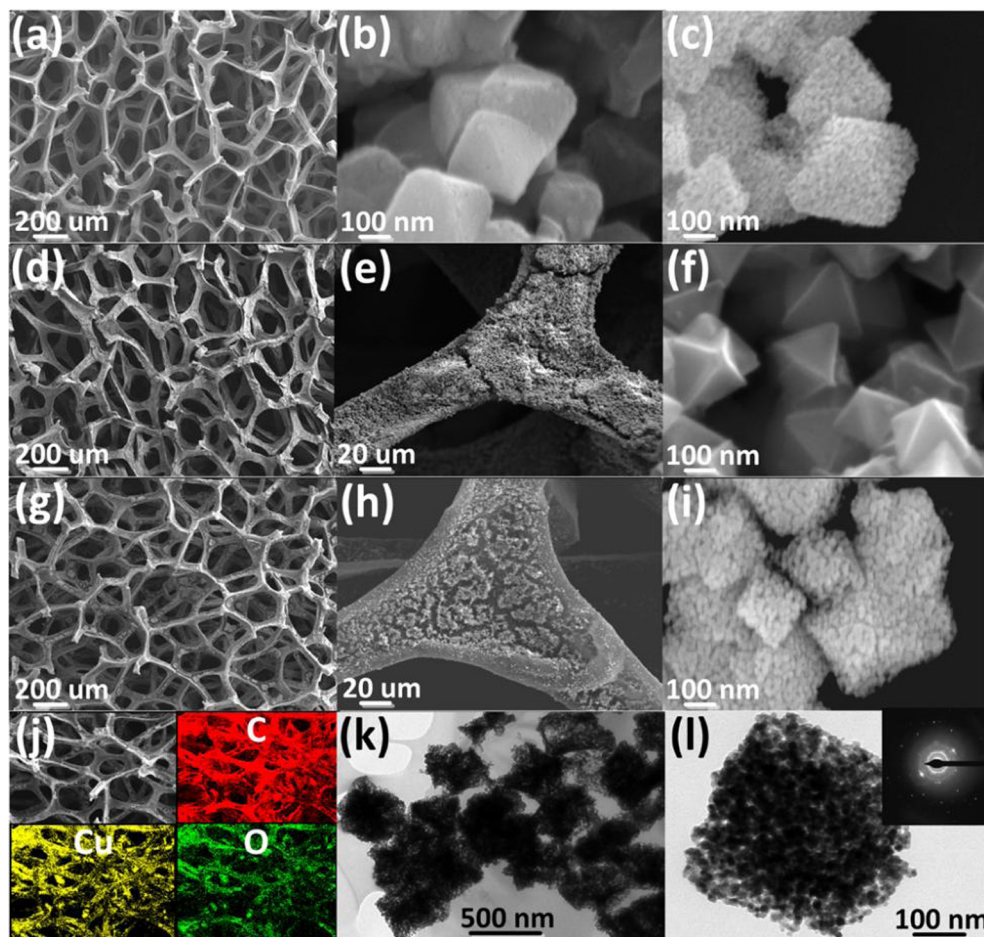
Fig. 3. SEM images of (a) 3DGN, (b) Cu-BTC, (c) CuO, (d, e, f) 3DGN/Cu-BTC and (g, h, i) 3DGN/CuO at different magnifications; (j) the EDS elemental mapping distribution of 3DGN/CuO; TEM images of (k) low- and (l) high-magnification CuO particles in 3DGN/CuO (the corresponding SAED pattern of CuO).

size and surface of MOF between bare MOF and the 3DGN/Cu-BTC composite. It can be seen that Cu-BTC particles in the composite have smaller size and more smooth and regular surface than that of the single Cu-BTC (Fig. 3f), suggesting that the unique feature of 3DGN has an influence on the self-assembly reaction of MOF precursors (Cu^{2+} ions and H_3BTC ligands), as observed in the MOF-graphene hybrids [62–64].

The control experiments were considered here. Clearly, the loading, morphology and size of MOF particles on the 3DGN substrate can be adjustable by controlling the concentration of MOF precursors during the in situ preparation process of the composite (Fig. S3). The results showed that MOF particles were sparsely distributed on the surface of 3DGN and these particles exhibited irregular shapes when the concentration of MOF precursors (H_3BTC, Cu salt) are much lower (1/5 time the current concentration). Then, the loading of MOF crystals increased and the morphology of MOF particles was close to the octahedral shape upon increasing the concentration of MOF precursors (1/2 time the current concentration). Also, the average size of MOF particles increased from about 150 nm to 300 nm. It should be noted that the loading of MOF has nearly reached its maximum and these particles changed completely to be octahedral when the 3DGN substrate was soaked into a saturated solution of H_3BTC ligand (MOF precursor). And the particle size of MOF at this concentration is similar to that of the sample with 1/2 time content. In this sense, the 3DGN substrate appeared to be a structure-directing agent for the nucleation and growth of MOF crystals. In addition, we found that the reaction time has no influence on the loading and morphology of MOF par-

ticles. Actually, if the immersion reaction time was further prolonged from 3.5 to 36 h, the loading and the morphology of MOF particles in the final composite remained almost unchanged.

After annealing 3DGN/Cu-BTC in air, the obtained 3DGN/CuO bulk material still kept the completeness (Fig. 3g). In addition, the color of the sample turned to black again, which was caused by high-temperature oxidation of MOF. These CuO particles have an average size of approximately 280 nm calculated from a statistical evaluation (Fig. S4). By a closer inspection of CuO particles, it was found that the CuO crystallites exhibited a typical porous octahedral structure containing numerous and discontinuous tiny CuO secondary nanocrystallites in size with a mean dimension of ca. 15 nm as estimated (Fig. S5) due to the release of gaseous molecules during the thermal conversion. Thus, this interparticle aggregation formed a mesoporous nanostructure, which will facilitate the Li-ion diffusion and make the maximum proportion of the surface accessible to the electrolyte. In our case, organic linkers in MOF can efficiently prevent the aggregation of the resulting nanometer particles in the primary octahedral MOF crystals, generating numerous voids in the final nano-octahedras with coarse surface. This result further confirmed that MOFs could be converted to the designed metal oxides with controlled morphologies and sizes through a proper thermal treatment [21,65]. The selected-area electron diffraction (SAED) pattern of CuO nano-octahedras in the composite showed well-defined multiple concentric circles, demonstrating the polycrystalline nature of nanostructures. The complete coverage of CuO layers can be further confirmed by energy-dispersive X-ray spectroscopy (EDS). The elemental

mapping images indicated the existence of carbon, oxygen and copper elements throughout the 3D macroporous graphene framework (Fig. 3j). Above results clearly validated that the CuO nanoparticles were uniformly anchored onto the framework of 3D graphene. In the control experiment, the composite of 3DGN and CuO has also been prepared by the physical mixing method. The interconnected porous framework of 3DGN collapsed when the ultrasonic mixing was applied during the preparation of a composite of the 3DGN substrate and as-prepared CuO particles. So, the 3DGN-CuO composite was synthesized by simply immersed 3DGN into the suspension of CuO octahedras without ultrasonic or stirring treatments. In this case, CuO particles in this physical mixed sample were scattered on the 3DGN substrate with obvious aggregations in some regions (Fig. S6). Importantly, the loading of CuO in this sample was much lower than that observed in the material prepared by in situ growth strategy. So, we can conclude that the designed fabrication process in this work facilitated the high loading of CuO as well as the formation of the special "wrapped in" structure of 3DGN/CuO, where the interfacial actions and the porous hierarchical structures have played key roles [66–69].

The textural feature of pure CuO has been investigated by nitrogen adsorption-desorption isotherms (Fig. S7). Pure CuO exhibited a typical type IV isotherm, where the approximately vertical rise of the curve at low-pressure region ($P/P_0 \sim 0$) suggested the existence of micropores, while the distinct hysteresis loop in the $P/P0$ range of 0.47–0.99 indicated the presence of mesopores. The BET specific surface area and pore volume of CuO was measured to be 7.16 $m^2\,g^{-1}$ and 1.65 $cm^3\,g^{-1}$, respectively, with the pore-size distribution maximum centered at around 16 nm. So, it can be expected from the texture data of pure CuO that the hierarchically interconnected and porous nanostructure of the final 3DGN/CuO composite will facilitate the mass diffusion of electrolyte and the fast transport of Li ion as well as buffer the volume variation of CuO particles.

The first three CV curves of the 3DGN/CuO composite electrode at a scan rate of 0.2 mV s^{-1} with the voltage window of 0.01–3.0 V were given in Fig. 4a. In combination with CV data of pure 3DGN and CuO, we can conclude all peaks observed in the composite originated from both components (Figs. S8a and S9a). The first cycle curve in the cathodic sweep was substantially different from the subsequent curves. During the first cathodic scan, four reduction peaks were observed at 1.10, 0.78, 0.30 and 0.11 V, respectively, which can be ascribed to a multi-step electrochemical reaction [70–76], involving (i) the formation of an intermediate Cu_2O phase, (ii) the decomposition of Cu_2O into Cu and Li_2O, (iii) some irreversible reaction, such as the formation of the SEI layer and electrolyte decomposition, (iv) the lithium intercalation/deintercalation between graphene layers. In the second cycle curve, the cathodic peaks slightly shifted towards higher voltages, while no significant changes in the peak positions and intensities were observed during the anodic scan. In the anodic process, two weak peaks located at 0.19 and 0.26 V were related to the decomposition of the SEI layer, whereas the well-defined strong peak at 2.43 V corresponded to the oxidation of Cu to Cu_2O and then further oxidation to CuO [76–79]. The electrochemical reaction involved in the charge-discharge process can be described as the following equations: $CuO + 2Li^+ + 2e^- \leftrightarrow Cu + Li_2O$ [80,81]. The third CV curves overlapped very well from the second cycle onwards, indicating a high reversibility of the redox reaction.

The 1st, 2nd, and 50th charge-discharge voltage profiles of the 3DGN/CuO electrode were performed at a current density of 100 mA g^{-1} in the voltage range of 0.01–3.0 V (versus Li^+/Li) (Fig. 4b). Obviously, the initial capacity of the 3DGN/CuO composite was higher significantly those of Cu-MOF and 3DGN/Cu-MOF materials (Fig. S10). It was also observed that the capacity of the 3DGN/CuO composite originated from the contribution of both

3DGN and CuO components (Figs. S8b and S9b). The first discharge and charge capacities of the composite were 569 and 422 mAh g^{-1}, respectively, yielding a high initial columbic efficiency of about 74%. The irreversible capacity loss arising during the first cycle mainly resulted from the diverse irreversible process such as interfacial lithium storage, inevitable formation of the solid electrolyte interface (SEI) layer and organic conductive polymer, as well as the electrolyte decomposition [29,75,82–85]. The subsequent columbic efficiency sharply increased to 94% and 99% in the 2nd and 50th cycles, respectively, indicating the good cycling stability of the 3DGN/CuO composite electrode. As shown in Fig. 4b, several voltage plateaus during the first charge-discharge process were clearly observed, associated with the multi-step electrochemical reaction during the conversion reaction between CuO and lithium. In the following 2nd and 50th cycles, some plateaus become broad or diminish, and the profiles almost overlap, in good agreement with above CV analyses. The 3DGN/CuO sample with low CuO loading was also prepared by changing the content (1/5 time the current concentration) of MOF crystals on the 3DGN surface, which revealed that a few CuO particles are scattered on the 3DGN substrate and most of 3DGN was not covered by CuO particles. The corresponding composite exhibited a lower capacity ($\sim$400 mAh g^{-1}) than that of the sample with high CuO loading, which can be ascribed to the low contribution of active material CuO. Above analysis further confirmed that the high CuO loading was benefit to improve the capacity of the final composite electrode.

The cycling performance of 3DGN/CuO and bare CuO electrodes at 100 mA g^{-1} is given in Fig. 4c. It is clearly noticed that the 3DGN/CuO composite electrode demonstrated a better capacity retention ability and cycling stability than that of bare CuO or 3DGN (Fig. S8c) electrode over 50 cycles. Except the large capacity loss of the first cycle for both electrodes, the second discharge capacity of CuO was 352 mAh g^{-1} and gradually decreased to 212 mAh g^{-1} after 50 discharge-charge cycles with a 60% capacity retention. This severe capacity decay of the CuO electrode can be attributed to the agglomeration and pulverization of CuO particles during the repeated lithiation and delithiation processes [19]. In contrast, the capacity of the 3DGN/CuO composite electrode was stable during the discharge-charge cycles and still retained at 405 mAh g^{-1} (a large areal capacity of 0.38 mAh cm^{-2}) at 100 mA g^{-1} after 50 cycles, which was almost 99% of the second reversible capacity (409 mAh g^{-1}). In addition, the Coulombic efficiency of the 3DGN/CuO electrode after cycling for 50 cycles remained at nearly 100%, indicating the fast stabilization of the ESI layer and high reversibility of the conversion reaction of Li and anode material. This result was superior to the oatmeal CuO, flower-like CuO, and pillow shaped porous CuO, and comparable with the CuO nanoparticles/graphene, CuO/C microspheres, but inferior to the nanoleaf-on-sheet CuO/graphene, leaf-like CuO/CNT and onion-like carbon coated CuO nanocapsules (see Table 1) [72,86–92]. The measured capacities of pure 3DGN and CuO were 390 and 379 mAh g^{-1} at 100 mA g^{-1}, respectively (Figs. S8b and S9b). The reversible capacity of 409 mAh g^{-1} at 100 mA g^{-1} observed in the 3DGN/CuO composite was lower than the theoretical value (674 mAh g^{-1}) of CuO. However, the capacity was higher than that (387 mAh g^{-1}) calculated based on the physical mixture of as-synthesized 3DGN (390 mAh g^{-1}) and CuO (379 mAh g^{-1}) as well as the content of each component in the hybrid. This enhanced capacity can be attributed to the synergistic effect between 3DGN and CuO materials.

The superior Li storage properties of the 3DGN/CuO composite electrode as compared to that of CuO electrode were supported by the electrochemical impedance spectra (EIS) measurements on the samples before and after 50 discharge-charge cycles (Fig. 4d). Before cycling, both impedance curves of CuO and
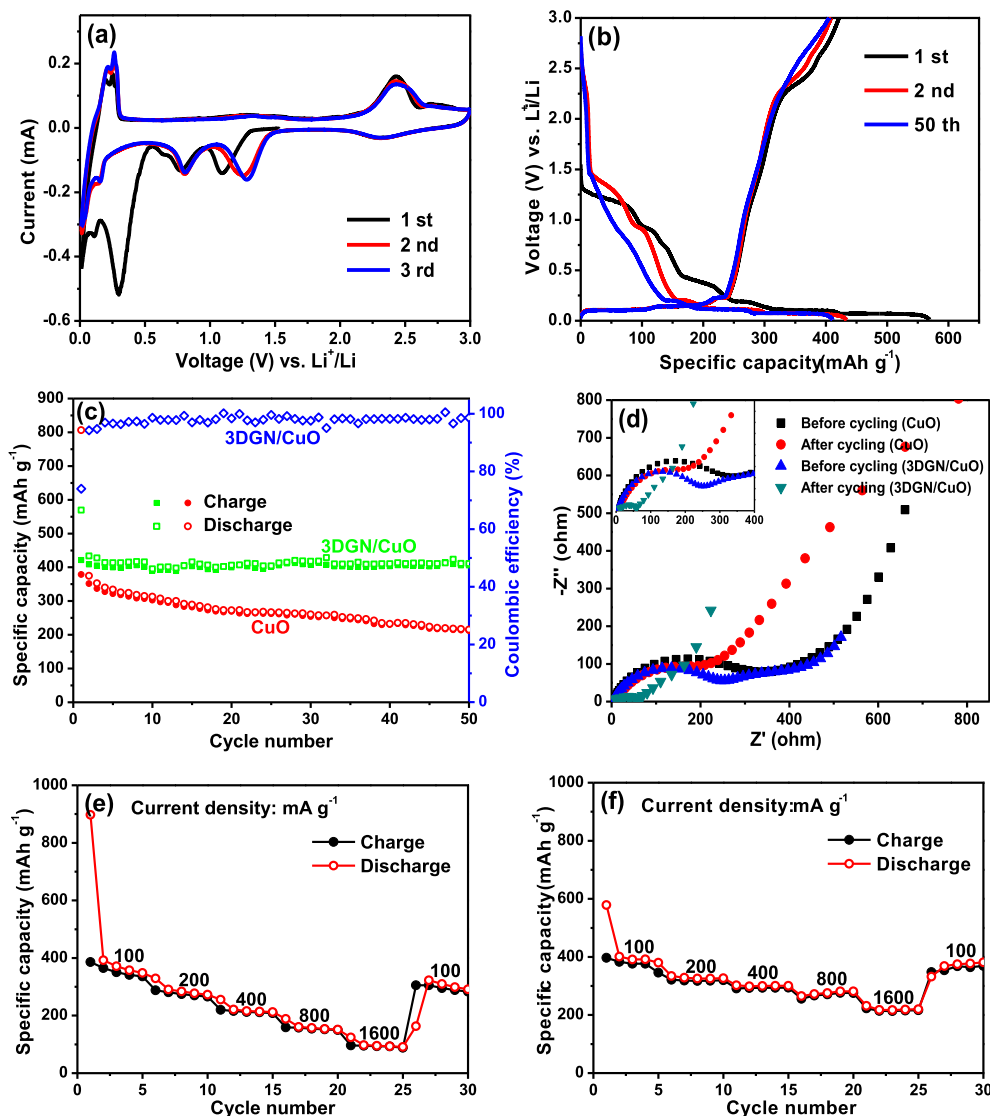
Fig. 4. (a) CV curves of 3DGN/CuO at a scan rate of 0.2 mV s⁻¹ in the potential range from 0.01–3.0 V vs Li/Li⁺, (b) charge–discharge curves of 3DGN/CuO at a current density of 100 mA g⁻¹, (c) comparison of cycling performances for 3DGN/CuO and bare CuO at 100 mA g⁻¹, (d) Nyquist plots of 3DGN/CuO and bare CuO electrodes before and after 50 cycles (Inset: Nyquist plots in the region of 0–400 ohm), and Rate capabilities of (e) bare CuO and (f) 3DGN/CuO electrodes at different current densities from 100 to 1600 mA g⁻¹.

Table 1
Comparison of specific capacities of our work with reported CuO, CuO-carbon electrode materials for LIBs.

Electrode materials	Current density (mA g⁻¹)	Cycle number	Specific capacity (mAh g⁻¹)	Refs
CuO octahedra/3DGN	100	50	405	This work
Oatmeal CuO	67	55	231.9	[86]
Flower-like CuO	67	50	392.4	[72]
Pillow shaped porous CuO	67	50	320	[87]
CuO nanoparticles/graphene	67	50	423	[88]
CuO/C microspheres	100	50	470	[89]
Nanoleaf-on-sheet CuO/graphene	100	50	600	[90]
Leaf-like CuO/CNT	60	50	627	[91]
Onion-like carbon coated CuO nanocapsules	100	50	628.7	[92]

3DGN/CuO showed a broad compressed semicircle in the high-frequency region corresponding to the interfacial resistance and charge-transfer kinetic-controlled region. Obviously, the diameter of the semicircle of the 3DGN/CuO composite electrode was smaller than that of the CuO electrode. This proved that the 3DGN/CuO electrode has a lower resistance for the interfacial electrochemical reaction, indicating the improved electrical conductivity and a more rapid charge transfer reaction with fast lithium ion diffusion after the incorporation of conductive 3DGN. The circle diameters of both 3DGN/CuO and CuO electrodes decreased after 50 cycles, demonstrating that the architectures of electrodes reached a stabilized state in the discharge–charge process.

The rate capabilities of bare CuO, 3DGN and 3DGN/CuO were evaluated at various current densities from 100 to 1600 mA g⁻¹

(Figs. 4e, f and S8d). The capacity retentions of 3DGN/CuO were 395, 328, 301, 277, and 219 mAh g^{-1} at 100, 200, 400, 800, and 1600 mA g^{-1}, respectively, exhibiting a better performance than those of bare CuO (357, 277, 212, 154 and 95 mAh g^{-1}) and 3DGN (376, 86, 84, 78 and 59 mAh g^{-1}) upon increasing the current densities. When the current rate was returned to 100 mA g^{-1}, the capacities of the composite electrode were resumed.

The above results clearly demonstrated the improved reversible specific capacity, remarkable cycle and rate performances of the 3DGN/CuO composite in contrast to pure CuO as an anode material for lithium storage, which can be reasonably attributed to the synergetic interaction between uniformly dispersed metal oxide nanoparticles and the 3D conductive graphene network [93–97]. Firstly, the interpenetrating meso-/macro-porous feature of 3DGN possessed an extremely highly accessible area, effectively preventing the aggregation of metal oxide nanoparticles, while the excellent electronic conductivity of the 3D graphene network was beneficial for the rapid transport and diffusion of electrolyte ions and electrons during the charge-discharge process. Secondly, the porous structures of 3D graphene network served as an elastic and stable buffer effectively alleviating/accommodating volume changes associated with metal oxides during lithium insertion and exaction process. Thirdly, the porous octahedral CuO composing of numerous and discontinuous tiny nanocrystallites enlarged the CuO/electrolyte contact area as well as provides more open interspaces and electrochemically active surface to accommodate lithium ions, and thus exhibited higher lithium-ion adsorption/desorption capacities. It should be noticed that 3DGN/CuO composite can be used directly to form ultralight and flexible electrode which can be applied to some special energy conversion/storage devices (e.g. light-weight LIBs, flexible LIBs, etc.).

4. Conclusions

In summary, a facile synthesis approach was proposed to fabricate well-defined metal oxide/3DGN hierarchical composites using MOF as the precursors of metal oxide and 3DGN as the matrix through an in-situ self-assembly, followed by a heat-treatment process. This self-standing 3DGN/CuO hybrid was used as light-weight and binder-free anode materials for lithium-ion battery, exhibiting a high gravimetric capacity and large reversible areal capacity, superior rate capacity and excellent cycling performance, which can be ascribed to the synergistic integration of 3DGN and CuO components. The design concept developed here may provide a general strategy to construct 3DGN/metal oxides composite structures for electrochemical energy storage and conversion applications.

Acknowledgments

Appendix A. Supplementary data

Supplementary data associated with this article can be found, in the online version, at http://dx.doi.org/10.1016/j.cej.2016.11.063.

References

[1] M. Armand, J.M. Tarascon, Building better batteries, Nature 451 (2008) 652–657.
[2] R. Mukherjee, R. Krishnan, T.M. Lu, N. Koratkar, Nanostructured electrodes for high-power lithium ion batteries, Nano Energy 1 (2012) 518–533.
[3] A.L.M. Reddy, M.M. Shaijumon, S.R. Gowda, P.M. Ajayan, Coaxial MnO$_2$/carbon nanotube array electrodes for high-performance lithium batteries, Nano Lett. 9 (2009) 1002–1006.
[4] F. Jiao, P.G. Bruce, Mesoporous crystalline β-MnO$_2$-a reversible positive electrode for rechargeable lithium batteries, Adv. Mater. 19 (2007) 657–660.
[5] S.H. Lee, S.H. Yu, J.E. Lee, A.H. Jin, D.J. Lee, N. Lee, H. Jo, K. Shin, T.Y. Ahn, Y.W. Kim, H. Choe, Y.E. Sung, T. Hyeon, Self-assembled Fe$_3$O$_4$ nanoparticle clusters as high-performance anodes for lithium ion batteries via geometric confinement, Nano Lett. 13 (2013) 4249–4256.
[6] J.P. Liu, Y.Y. Li, H.J. Fan, Z.H. Zhu, J. Jiang, R.M. Ding, Y.Y. Hu, X.T. Huang, Iron oxide-based nanotube arrays derived from sacrificial template-accelerated hydrolysis: large-area design and reversible lithium storage, Chem. Mater. 22 (2010) 212–217.
[7] B. Wang, J.S. Chen, H.B. Wu, Z.Y. Wang, X.W. Lou, Quasiemulsion-templated formation of α-Fe$_2$O$_3$ hollow spheres with enhanced lithium storage properties, J. Am. Chem. Soc. 133 (2011) 17146–17148.
[8] S.L. Liu, L.N. Zhang, J.P. Zhou, J.F. Xiang, J.T. Sun, J.G. Guan, Fiberlike Fe$_2$O$_3$ macroporous nanomaterials fabricated by calcinating regenerate cellulose composite fibers, Chem. Mater. 20 (2008) 3623–3628.
[9] O. Waser, M. Hess, A. Güntner, P. Novók, S.E. Pratsinis, Size controlled CuO nanoparticles for Li-ion batteries, J. Power Sources 241 (2013) 415–422.
[10] J.C. Park, J. Kim, H. Kwon, H. Song, Gram-scale synthesis of Cu$_2$O nanocubes and subsequent oxidation to CuO hollow nanostructures for lithium-ion battery anode materials, Adv. Mater. 21 (2009) 803–807.
[11] M. Sasidharan, N. Gunawardhana, C. Senthil, M. Yoshio, Micelle templated NiO hollow nanospheres as anode materials in lithium ion batteries, J. Mater. Chem. A 2 (2014) 7337–7344.
[12] J.M. Ma, J.Q. Yang, L.F. Jiao, Y.H. Mao, T.H. Wang, X.C. Duan, J.B. Lian, W.J. Zheng, NiO nanomaterials: controlled fabrication, formation mechanism and the application in lithium-ion battery, CrystEngComm 14 (2012) 453–459.
[13] Z.Y. Wang, D.Y. Luan, F.Y.C. Boey, X.W. Lou, Fast formation of SnO$_2$ nanoboxes with enhanced lithium storage capability, J. Am. Chem. Soc. 133 (2011) 4738–4741.
[14] R. Demir-Cakan, Y.S. Hu, M. Antonietti, J. Maier, M.M. Titirici, Facile one-pot synthesis of mesoporous SnO$_2$ microspheres via nanoparticles assembly and lithium storage properties, Chem. Mater. 20 (2008) 1227–1229.
[15] L.M. Zhang, B. Yan, J.H. Zhang, Y.J. Liu, A.H. Yuan, G. Yang, Design and self-assembly of metal-organic framework-derived porous Co$_3$O$_4$ hierarchical structures for lithium-ion batteries, Ceram. Int. 42 (2016) 5160–5170.
[16] B. Yan, L. Chen, Y.J. Liu, G.X. Zhu, C.G. Wang, H. Zhang, G. Yang, H.T. Ye, A.H. Yuan, Co$_3$O$_4$ nanostructures with a high rate performance as anode materials for lithium-ion batteries, prepared via book-like cobalt-organic frameworks, CrystEngComm 16 (2014) 10227–10234.
[17] J.S. Chen, Y.L. Tan, C.M. Li, Y.L. Cheah, D.Y. Luan, S. Madhavi, F.Y.C. Boey, L.A. Archer, X.W. Lou, Constructing hierarchical spheres from large ultrathin anatase TiO$_2$ nanosheets with nearly 100% exposed (0 0 1) facets for fast reversible lithium storage, J. Am. Chem. Soc. 132 (2010) 6124–6130.
[18] Y.S. Hu, L. Kienle, Y.G. Guo, J. Maier, High lithium electroactivity of nanometer-sized rutile TiO$_2$, Adv. Mater. 18 (2006) 1421–1426.
[19] J.J. Zhang, A.S. Yu, Nanostructured transition metal oxides as advanced anodes for lithium-ion batteries, Sci. Bull. 60 (2015) 823–838.
[20] C. Liang, M.X. Gao, H.G. Pan, Y.F. Liu, M. Yan, Lithium alloys and metal oxides as high-capacity anode materials for lithium-ion batteries, J. Alloys Compd. 575 (2013) 246–256.
[21] W. Xia, A. Mahmood, R.Q. Zou, Q. Xu, Metal-organic frameworks and their derived nanostructures for electrochemical energy storage and conversion, Energy Environ. Sci. 8 (2015) 1837–1866.
[22] L.M. Zhang, J.H. Zhang, Y.J. Liu, L. Zhang, A.H. Yuan, Porous ZnO/NiO microspherical structures prepared by thermolysis of heterobimetallic metal-organic framework as supercapacitor electrodes, J. Nanosci. Nanotechnol. 16 (2016), http://dx.doi.org/10.1166/jnn.2016.12677.
[23] J. Wang, Y. Zhang, X.Q. Liu, J. Xiao, H. Zhou, A.H. Yuan, Two Zn(II) and Co(II) coordination compounds based on polycarboxylates and curved 4,4′-azopyridine ligands, Microporous. Mesoporous. Mater. 159 (2012) 100–104.
[24] Y. Zhang, J. Wang, X.F. Yan, X.Q. Liu, H. Zhou, A.H. Yuan, Syntheses, structures, thermal stabilities and gas sorption properties of two rod-based microporous lead(II) polycarboxylate coordination frameworks, Microporous. Mesoporous. Mater. 184 (2014) 15–20.
[25] P. Pachfule, D. Shinde, M. Majumder, Q. Xu, Fabrication of carbon nanorods and graphene nanoribbons from a metal-organic framework, Nat. Chem. 8 (2016) 718–724.
[26] A. Mahmood, W.H. Guo, H. Tabassum, R.Q. Zou, Metal-organic framework-based nanomaterials for electrocatalysis, Adv. Energy Mater. 6 (2016) 1600423.
[27] J.K. Sun, Q. Xu, Functional materials derived from open framework templates/precursors: synthesis and applications, Energy Environ. Sci. 7 (2014) 2071–2100.
[28] B. Liu, H. Shioyama, T. Akita, Q. Xu, Metal-organic framework as a template for porous carbon synthesis, J. Am. Chem. Soc. 130 (2008) 5390–5391.

[29] X. Xu, R. Cao, S. Jeong, J. Cho, Spindle-like mesoporous α-Fe$_2$O$_3$ anode material prepared from MOF template for high-rate lithium batteries, Nano Lett. 12 (2012) 4988–4991.

[30] J. Shao, Z.M. Wan, H.M. Liu, H.Y. Zheng, T. Gao, M. Shen, Q.T. Qu, H.H. Zheng, Metal organic frameworks-derived Co$_3$O$_4$ hollow dodecahedrons with controllable interiors as outstanding anodes for Li storage, J. Mater. Chem. A 2 (2014) 12194–12200.

[31] R.B. Wu, X.K. Qian, X.H. Rui, H. Liu, B.L. Yadian, K. Zhou, J. Wei, Q.Y. Yan, X.Q. Feng, Y. Long, L.Y. Wang, Y.Z. Huang, Zeolitic imidazolate framework 67-derived high symmetric porous Co$_3$O$_4$ hollow dodecahedra with highly enhanced lithium storage capability, Small 10 (2014) 1932–1938.

[32] R.B. Wu, X.K. Qian, F. Yu, H. Liu, K. Zhou, J. Wei, Y.Z. Huang, MOF-templated formation of porous CuO hollow octahedra for lithium-ion battery anode materials, J. Mater. Chem. A 1 (2013) 11126–11129.

[33] Z.Q. Wang, X. Li, H. Xu, Y. Yang, Y.J. Cui, H.G. Pan, Z.Y. Wang, B.L. Chen, G.D. Qian, Porous anatase TiO$_2$ constructed from a metal-organic framework for advanced lithium-ion battery anodes, J. Mater. Chem. A 2 (2014) 12571–12575.

[34] T. Song, H. Han, H. Choi, J.W. Lee, H. Park, S. Lee, W.I. Park, S. Kim, L. Liu, U. Paik, TiO$_2$ nanotube branched tree on a carbon nanofiber nanostructure as an anode for high energy and power lithium ion batteries, Nano Research 7 (2014) 491–501.

[35] M. Zhang, E. Uchaker, S. Hu, Q.F. Zhang, T.H. Wang, G.Z. Cao, J.Y. Li, CoO-carbon nanofiber networks prepared by electrospinning as binder-free anode materials for lithium-ion batteries with enhanced properties, Nanoscale 5 (2013) 12342–12349.

[36] G. Huang, F.F. Zhang, X.C. Du, Y.L. Qin, D.M. Yin, L.M. Wang, Metal organic frameworks route to in situ insertion of multiwalled carbon nanotubes in Co$_3$O$_4$ polyhedra as anode materials for lithium-ion batteries, ACS Nano 9 (2015) 1592–1599.

[37] D. Gu, W. Li, F. Wang, H. Bongard, B. Spliethoff, W. Schmidt, C. Weidenthaler, Y. Y. Xia, D.Y. Zhao, F. Schuth, Controllable synthesis of mesoporous peapod-like Co$_3$O$_4$@Carbon nanotube arrays for high-performance lithium-ion batteries, Angew. Chem. Int. Ed. 54 (2015) 7060–7064.

[38] Y. Wu, Y. Wei, J.P. Wang, K.L. Jiang, S.S. Fan, Conformal Fe$_3$O$_4$ sheath on aligned carbon nanotube scaffolds as high-performance anodes for lithium ion batteries, Nano Lett. 13 (2013) 818–823.

[39] J.T. Zai, X.F. Qian, Three dimensional metal oxides-graphene composites and their applications in lithium ion batteries, RSC Adv. 5 (2015) 8814–8834.

[40] Z.Y. Ji, X.P. Shen, G.X. Zhu, H. Zhou, A.H. Yuan, Reduced graphene oxide/nickel nanocomposites: facile synthesis, magnetic and catalytic properties, J. Mater. Chem. 22 (2012) 3471–3477.

[41] S. Bai, X.P. Shen, G.X. Zhu, A.H. Yuan, J. Zhang, Z.Y. Ji, D.Z. Qiu, The influence of wrinkling in reduced graphene oxide on their adsorption and catalytic properties, Carbon 60 (2013) 157–168.

[42] Z.Y. Ji, J.L. Zhao, X.P. Shen, X.Y. Yue, A.H. Yuan, H. Zhou, J. Yang, Construction of magnetically separable Ag$_3$PO$_4$/Fe$_3$O$_4$/GO composites as recyclable photocatalysts, Ceram. Int. 41 (2015) 13509–13515.

[43] X.Q. Cai, X.P. Shen, L.B. Ma, Z.Y. Ji, C. Xu, A.H. Yuan, Solvothermal synthesis of NiCo-layered double hydroxide nanosheets decorated on RGO sheets for high performance supercapacitor, Chem. Eng. J. 268 (2015) 251–259.

[44] X.H. Xia, D.L. Chao, Y.Q. Zhang, Z.X. Shen, H.J. Fan, Three-dimensional graphene and their integrated electrodes, Nano Today 9 (2014) 785–807.

[45] B. Luo, L.J. Zhi, Design and construction of three dimensional graphene-based composites for lithium ion battery applications, Energy Environ. Sci. 8 (2015) 456–477.

[46] X.H. Cao, B. Zheng, X.H. Rui, W.H. Shi, Q.Y. Yan, H. Zhang, Metal oxide-coated three-dimensional graphene prepared by the use of metal-organic frameworks as precursors, Angew. Chem. Int. Ed. 53 (2014) 1404–1409.

[47] D. Ji, H. Zhou, J. Zhang, Y.Y. Dan, H.X. Yang, A.H. Yuan, Facile synthesis of a metal-organic framework-derived Mn$_2$O$_3$ nanowire coated three-dimensional graphene network for high-performance free-standing supercapacitor electrodes, J. Mater. Chem. A 4 (2016) 8283–8290.

[48] H. Zhou, J. Zhang, D. Ji, A.H. Yuan, X.P. Shen, Effect of catalyst loading on hydrogen storage capacity of ZIF-8/graphene oxide doped with Pt or Pd via spillover, Microporous. Mesoporous. Mater. 229 (2016) 68–75.

[49] H. Zhou, J. Zhang, J. Zhang, X.F. Yan, X.P. Shen, A.H. Yuan, High-capacity room-temperature hydrogen storage of zeolitic imidazolate framework/graphene oxide promoted by platinum metal catalyst, Int. J. Hydrogen Energy 40 (2015) 12275–12285.

[50] H. Zhou, X.Q. Liu, J. Zhang, X.F. Yan, Y.J. Liu, A.H. Yuan, Enhanced room-temperature hydrogen storage capacity in Pt-loaded graphene oxide/HKUST-1 composites, Int. J. Hydrogen Energy 39 (2014) 2160–2167.

[51] J. Zhang, X.Q. Liu, H. Zhou, X.F. Yan, Y.J. Liu, A.H. Yuan, Pt-doped graphene oxide/MIL-101 nanocomposites exhibiting enhanced hydrogen uptake at ambient temperature, RSC Adv. 4 (2014) 28908–28913.

[52] J.L. Zhuang, D. Ceglarek, S. Pethuraj, A. Terfort, Rapid room-temperature synthesis of metal-organic framework HKUST-1 crystals in bulk and as oriented and patterned thin films, Adv. Funct. Mater. 21 (2011) 1442–1447.

[53] A.C. Ferrari, Raman spectroscopy of graphene and graphite: disorder, electron–phonon coupling, doping and nonadiabatic effects, Solid State Commun. 143 (2007) 47–57.

[54] D. Graf, F. Molitor, K. Ensslin, C. Stampfer, A. Jungen, C. Hierold, L. Wirtz, Spatially resolved Raman spectroscopy of single-and few-layer graphene, Nano Lett. 7 (2007) 238–242.

[55] Z.H. Xue, M.Q. Li, H.H. Rao, B. Yin, X.B. Zhou, X.H. Liu, X.Q. Lu, Phase transformation-controlled synthesis of CuO nanostructures and their application as an improved material in a carbon-based modified electrode, RSC Adv. 6 (2016) 12829–12836.

[56] X.Q. Wang, G.C. Xi, S.L. Xiong, Y.K. Liu, B.J. Xi, W.C. Yu, Y.T. Qian, Solution-phase synthesis of single-crystal CuO nanoribbons and nanorings, Cryst. Growth Des. 7 (2007) 931–934.

[57] Z.H. Li, M.F. Shao, L. Zhou, R.K. Zhang, C. Zhang, J.B. Han, M. Wei, D.G. Evans, X. Duan, A flexible all-solid-state micro-supercapacitor based on hierarchical CuO@layered double hydroxide core–shell nanoarrays, Nano Energy 20 (2016) 294–304.

[58] Y. Lu, H.L. yan, K.W. Qiu, J.B. Cheng, W.X. Wang, X.M. Liu, C.C. Tang, J.K. Kim, Y. S. Luo, Hierarchical porous CuO nanostructures with tunable properties for high performance supercapacitors, in: RSC Adv. 5 (2015) 10773–10781.

[59] G.D. Ruan, Z.Z. Sun, Z.W. Peng, J.M. Tour, Growth of graphene from food, insects, and waste, ACS Nano 5 (2011) 7601–7607.

[60] D.Q. Gao, G.J. Yang, J.Y. Li, J.Z. Zhang, J.L. Zhang, D.S. Xue, Room-temperature ferromagnetism of flowerlike CuO nanostructures, J. Phys. Chem. C 114 (2010) 18347–18351.

[61] H.C. Schniepp, J.L. Li, M.J. McAllister, H. Sai, M. Herrera-Alonso, D.H. Adamson, R.K. Pru'homme, R. Car, D.A. Saville, I.A. Aksay, Functionalized single graphene sheets derived from splitting graphite oxide, J. Phys. Chem. B 110 (2006) 8535–8539.

[62] S. Liu, L.X. Sun, F. Xu, J. Zhang, C.L. Jiao, F. Li, Z.B. Li, S. Wang, Z.Q. Wang, X. Jiang, H.Y. Zhou, L.N. Yang, C. Schick, Nanosized Cu-MOFs induced by graphene oxide and enhanced gas storage capacity, Energy Environ. Sci. 6 (2013) 818–823.

[63] M. Jahan, Q.L. Bao, J.X. Yang, K.P. Loh, Structure-directing role of graphene in the synthesis of metal-organic framework nanowire, J. Am. Chem. Soc. 132 (2010) 14487–14495.

[64] C. Petit, T.J. Bandosz, MOF–graphite oxide composites: combining the uniqueness of graphene layers and metal–organic frameworks, Adv. Mater. 21 (2009) 4753–4757.

[65] L. Lux, K. Williams, S.Q. Ma, Heat-treatment of metal–organic frameworks for green energy applications, CrystEngComm 17 (2015) 10–22.

[66] X.M. Li, J.T. Zai, S.J. Xiang, Y.Y. Liu, X.B. He, Z.Y. Xu, K.X. Wang, Z.F. Ma, X.F. Qian, Regeneration of metal sulfides in the delithiation process: the key to cyclic stability, Adv. Energy Mater. 6 (2016) 1601056.

[67] B. Li, X.M. Li, J.T. Zai, X.F. Qian, Facile synthesis of porous Zn-Sn-O nanocubes and their electrochemical performance, Nano-Micro Lett. 8 (2016) 174–181.

[68] Y.L. Xiao, X.M. Li, J.T. Zai, K.X. Wang, Y. Gong, B. Li, Q.Y. Han, X.F. Qian, CoFe$_2$O$_4$-graphene nanocomposites synthesized through an ultrasonic method with enhanced performances as anode materials for Li-ion batteries, Nano-Micro Lett. 6 (2014) 307–315.

[69] L.Q. Tao, J.T. Zai, K.X. Wang, H.J. Zhang, M. Xu, J. Shen, Y.Z. Su, X.F. Qian, Co$_3$O$_4$ nanorods/graphene nanosheets nanocomposites for lithium ion batteries with improved reversible capacity and cycle stability, J. Power Sources 202 (2012) 230–235.

[70] Z.C. Bai, Y.W. Zhang, Y.H. Zhang, C.L. Guo, B. Tang, A large-scale, green route to synthesize of leaf-like mesoporous CuO as high-performance anode materials for lithium ion batteries, Electrochim. Acta 159 (2015) 29–34.

[71] J. Wang, Y.C. Liu, S.Y. Wang, X.T. Guo, Y.P. Liu, Facile fabrication of pompon-like hierarchical CuO hollow microspheres for high-performance lithium-ion batteries, J. Mater. Chem. A 2 (2014) 1224–1229.

[72] C. Wang, D.C. Higgins, F.F. Wang, G. Wu, Controlled synthesis of micro/nanostructured CuO anodes for lithium-ion batteries, Nano Energy 9 (2014) 334–344.

[73] Z.Y. Wang, F.B. Su, S. Madhavi, X.W. Lou, CuO nanostructures supported on Cu substrate as integrated electrodes for highly reversible lithium storage, Nanoscale 3 (2011) 1618–1623.

[74] E. Garcia-Tamayo, M.V.U. Locati, D. Munao, E.M. Kelder, Nanostructured Fe$_2$O$_3$ and CuO composite electrodes for Li ion batteries synthesized and deposited in one step, J. Power Sources 196 (2011) 6425–6432.

[75] J.Y. Xiang, J.P. Tu, Y.Q. Qiao, X.L. Wang, J. Zhong, D. Zhang, C.D. Gu, Electrochemical impedance analysis of a hierarchical CuO electrode composed of self-assembled nanoplates, J. Phys. Chem. C 115 (2011) 2505–2513.

[76] S.Q. Wang, J.Y. Zhang, C.H. Chen, Dandelion-like hollow microspheres of CuO as anode material for lithium-ion batteries, Scr. Mater. 57 (2007) 337–340.

[77] L. Martin, H. Martinez, D. Poinot, B. Pecquenard, F.L. Cras, Comprehensive X-ray photoelectron spectroscopy study of the conversion reaction mechanism of CuO in lithiated thin film electrodes, J. Phys. Chem. C 117 (2013) 4421–4430.

[78] X. Wang, D.M. Tang, H.Q. Li, W. Yi, T.Y. Zhai, Y. Bando, D. Golberg, Revealing the conversion mechanism of CuO nanowires during lithiation-delithiation by in situ transmission electron microscopy, Chem. Commun. 48 (2012) 4812–4814.

[79] R. Sahay, P.S. Kumar, V. Aravindan, J. Sundaramurthy, W.C. Ling, S.G. Mhausalkar, S. Ramakrishna, S. Madhavi, High aspect ratio electrospun CuO nanofibers as anode material for lithium-ion batteries with superior cycleability, J. Phys. Chem. C 116 (2012) 18087–18092.

[80] A. Debart, L. Dupont, P. Poizot, J.B. Leriche, J.M. Tarascon, A transmission electron microscopy study of the reactivity mechanism of tailor-made CuO particles toward lithium, CuO cathode in lithium cells-II. Reduction mechanism of CuO, J. Electrochem. Soc. 148 (2001) A1266–A1274.

[81] P. Novak, CuO cathode in lithium cells-II. Reduction mechanism of CuO, Electrochim. Acta 30 (1985) 1687–1692.

[82] S. Mohapatra, S.V. Nair, D. Santhanagopalan, A.K. Rai, Nanoplate and mulberry-like porous shape of CuO as anode materials for secondary lithium ion battery, Electrochim. Acta 206 (2016) 217–225.

[83] Y. Liu, W. Wang, L. Gu, Y.W. Wang, Y.L. Ying, Y.Y. Mao, L.W. Sun, X.S. Peng, Flexible CuO nanosheets/reduced-graphene oxide composite paper: binder-free anode for high-performance lithium-ion batteries, ACS Appl. Mater. Interfaces 5 (2013) 9850–9855.

[84] J.Y. Xiang, J.P. Tu, L. Zhang, Y. Zhou, X.L. Wang, S.J. Shi, Self-assembled synthesis of hierarchical nanostructured CuO with various morphologies and their application as anodes for lithium ion batteries, J. Power Sources 195 (2010) 313–319.

[85] S.F. Zheng, J.S. Hu, L.S. Zhong, W.G. Song, L.J. Wan, Y.G. Guo, Introducing dual functional CNT networks into CuO nanomicrospheres toward superior electrode materials for lithium-ion batteries, Chem. Mater. 20 (2008) 3617–3622.

[86] C. Wang, Q. Li, F.F. Wang, G.F. Xia, R.Q. Liu, D.Y. Li, N. Li, J.S. Spendelow, G. Wu, Morphology-dependent performance of CuO anodes via facile and controllable synthesis for lithium-ion batteries, ACS Appl. Mater. Interfaces 6 (2014) 1243–1250.

[87] W. Mei, J. Dalai, F. Ran, S. Limin, G. Mingxia, Y. Linhai, Pillow-shaped porous CuO as anode material for lithium-ion batteries, Inorg. Chem. Commun. 14 (2011) 38–41.

[88] Y.J. Mai, X.L. Wang, J.Y. Xiang, Y.Q. Qiao, D. Zhang, C.D. Gu, J.P. Tu, CuO/graphene composite as anode materials for lithium-ion batteries, Electrochim. Acta 56 (2011) 2306–2311.

[89] X.H. Huang, C.B. Wang, S.Y. Zhang, F. Zhou, CuO/C microspheres as anode materials for lithium ion batteries, Electrochim. Acta 56 (2011) 6752–6756.

[90] X.Y. Zhou, J. Zhang, Q.M. Su, J.J. Shi, Y. Liu, G.H. Du, Nanoleaf-on-sheet CuO/graphene composites: Microwave-assisted assemble and excellent electrochemical performances for lithium ion batteries, Electrochim. Acta 125 (2014) 615–621.

[91] J.Y. Xiang, J.P. Tu, J. Zhang, D. Zhang, J.P. Cheng, Incorporation of MWCNTs into leaf-like CuO nanoplates for superior reversible Li-ion storage, Electrochem. Commun. 12 (2010) 1103–1107.

[92] X.G. Liu, N.N. Bi, C. Feng, S.W. Or, Y.P. Sun, C.G. Jin, W.H. Li, F. Xiao, Onion-like carbon coated CuO nanocapsules: a highly reversible anode material for lithium ion batteries, J. Alloys Compd. 587 (2014) 1–5.

[93] C.F. Zhang, J.S. Yu, Morphology-tuned synthesis of NiCo$_2$O$_4$-coated 3D graphene architectures used as binder-free electrodes for lithium-ion batteries, Chem. Eur. J. 22 (2016) 4422–4430.

[94] R. Tian, Y.Y. Zhang, Z.H. Chen, H.N. Duan, B.Y. Xu, Y.P. Guo, H.M. Kang, H. Li, H.Z. Liu, The effect of annealing on a 3D SnO$_2$/graphene foam as an advanced lithium-ion battery anode, Sci. Rep. 6 (2016) 19195.

[95] Z.Y. Sui, C.Y. Wang, K.W. Shu, Q.S. Yang, Y. Ge, G.G. Wallace, B.H. Han, Manganese dioxide-anchored three-dimensional nitrogen-doped graphene hybrid aerogels as excellent anode materials for lithium ion batteries, J. Mater. Chem. A 3 (2015) 10403–10412.

[96] Z.X. Huang, Y. Wang, Y.G. Zhu, Y.M. Shi, J.I. Wong, H.Y. Yang, 3D graphene supported MoO$_2$ for high performance binder-free lithium ion battery, Nanoscale 6 (2014) 9839–9845.

[97] J.S. Luo, J.L. Liu, Z.Y. Zeng, C.F. Ng, L.J. Ma, H. Zhang, J.Y. Lin, Z.X. Shen, H.J. Fan, Three-dimensional graphene foam supported Fe$_3$O$_4$ lithium battery anodes with long cycle life and high rate capability, Nano Lett. 13 (2013) 6136–6143.